

Testing strong line metallicity diagnostics at $z \sim 2$

V. Patrício,^{1*} L. Christensen,¹ H. Rhodin¹, R. Cañameras¹ and M. A. Lara-López¹

¹ *Dark Cosmology Centre, Niels Bohr Institute, University of Copenhagen, Juliane Maries Vej 30, 2100 Copenhagen, Denmark*

Accepted XXX. Received YYY; in original form ZZZ

ABSTRACT

High- z galaxy gas-phase metallicities are usually determined through observations of strong optical emission lines with calibrations tied to the local universe. Recent debate has questioned if these calibrations are valid in the high- z universe. We investigate this by analysing a sample of 16 galaxies at $z \sim 2$ available in the literature, and for which the metallicity can be robustly determined using oxygen auroral lines. The sample spans a redshift range of $1.4 < z < 3.6$, has metallicities of 7.4–8.4 in $12+\log(\text{O}/\text{H})$ and stellar masses $\sim 10^{7.5-11} M_{\odot}$. We test commonly used strong line diagnostics ($R23$, $O3$, $O2$, $O32$, $N2$, $O3N2$ and $Ne3O2$) as prescribed by four different sets of empirical calibrations, as well as one fully theoretical calibration. We find that none of the strong line diagnostics (or calibration set) tested perform consistently better than the others. Amongst the line ratios tested, $R23$ and $O3$ deliver the best results, with accuracies as good as 0.01–0.04 dex and dispersions of ~ 0.2 dex in two of the calibrations tested. Generally, line ratios involving nitrogen predict higher values of metallicity, while results with $O32$ and $Ne3O2$ show large dispersions. The theoretical calibration yields an accuracy of 0.06 dex, comparable to the best strong line methods. We conclude that, within the metallicity range tested in this work, the locally calibrated diagnostics can still be reliably applied at $z \sim 2$. However, we caution that for $\sim 60\%$ of our sample the observed $R23$ line ratios were out of the range of applicability of some of the calibrations tested.

Key words: galaxies: abundances – galaxies: high-redshift – galaxies: fundamental parameters

1 INTRODUCTION

One of the fundamental steps to understand the processes of galaxy growth and evolution is to robustly determine the chemical enrichment of galaxies over cosmic time. Gas-phase oxygen abundances (hereafter *metallicity*) can be determined from a range of diagnostics tools applied to emission lines. Generally, these tools rely on strong optical emission lines and on empirical abundance diagnostics, such as the $R23$ (Pagel et al. 1979), $O3N2$ and $N2$ (Pettini & Pagel 2004) ratios. It has long been known that these independently calibrated diagnostics are not compatible with each other, differing up to ~ 0.15 dex (Kewley & Ellison 2008), which translates in a change of the mass-metallicity relation y -intercept of up to 0.7 dex in the local Universe (Kewley & Ellison 2008) and about 0.3 dex at $z \sim 0.6$ (Maiolino et al. 2008).

Efforts have been made to derive consistent calibrations, but these studies rely mainly on local or low-redshift samples (e.g. Izotov et al. 2006; Pettini & Pagel 2004). On the

high- z regime, there are concerns that strong-line diagnostics such as $N2$ do not deliver reliable metallicities, since $N2$ is sensitive to the variation of the N/O ratio and to the ionisation parameter, and there are strong indications that ionisation parameter change through cosmic time (Steidel et al. 2014; Kewley et al. 2015). The effort to validate the local metallicity diagnostics has been extended up to $z \sim 1$ (Ly et al. 2016; Jones et al. 2015), but considering the number of surveys currently measuring galaxy metallicities at $z \sim 2$ with KMOS (Wisnioski et al. 2015) and MOSFIRE (Steidel et al. 2014), and the upcoming JWST spectra of high-redshift galaxies, it is timely to expand the metallicity diagnostics calibration to even higher redshifts.

The most direct method to determine metallicity relies only on atomic physics to calculate abundances. The intensity of an emission line depends on the abundance of the ion that it originates from, which we wish to determine, but also on the probability of that particular transition to occur, either through collisions or de-excitation, which is determined by atomic physics (see, for example, Osterbrock 1989). This probability can be precisely calculated if the electron temperature and density are known. In this case, the several ion

* E-mail: vera.patricio@dark-cosmology.dk

abundances of an element can be calculated and summed to obtain the total abundance. This method is called the *direct method* (T_e) and it is the base of most empirical calibrations.

The electron temperature can be determined using line ratios involving auroral emission lines such as [O III] $\lambda 4364$ or [N II] $\lambda 5755$ (e.g. [Izotov et al. 2006](#)). These auroral lines become increasingly faint in lower-temperature H II regions in high-mass ($\log M_* > 10.0$) and high-metallicity ($Z/Z_\odot > 0.5$) galaxies, that are most frequently targeted in surveys. Conversely, low-mass galaxies have higher ionisation parameters, higher temperatures and UV lines become increasingly bright compared with more massive galaxies, but the intrinsic faintness of low-mass galaxies makes them challenging targets. This makes the detection of auroral lines very challenging, even in the local Universe. For example, of the original 1 200 000 galaxies from SDSS DR7, only 400 ($\sim 0.03\%$) had detections ([Pilyugin et al. 2010](#)). At high- z , the detection of these lines becomes increasingly challenging and time consuming even on the largest aperture telescopes and the direct method is rarely used.¹ By targeting strongly lensed sources, which can have their flux magnified by a foreground massive galaxy cluster or massive galaxy up to a factor of >10 , we can examine galaxies that are intrinsically fainter than those studied in flux-limited surveys.

Strongly lensed galaxies at $z \sim 2$ are still relatively rare, but observational efforts in the past decade have resulted in a sample of about two dozens of objects where auroral lines can be detected (e.g. [Yuan & Kewley 2009](#); [Dessauges-Zavadsky et al. 2010](#); [Christensen et al. 2012a,b](#); [James et al. 2014](#); [Steidel et al. 2014](#)). Using these literature data, we assembled a sample of 16 galaxies at $z \sim 2$, mostly lensed, where metallicities can both be derived through the direct and strong line methods, and use this sample to test the validity of commonly used strong line diagnostics.

This paper is structured as follows. We describe our sample in Section 2. In Section 3, we homogeneously re-derive the electron temperature for the entire sample. In Section 4, we derive the oxygen abundance based on the retrieved electron temperatures applying the direct method, and in Section 5 and 6 we compare these results with what is obtained using commonly used empirical and theoretical calibrations and finish with a summary and conclusions in Section 7.

We adopt a solar metallicity of $12+\log(\text{O}/\text{H}) = 8.69$ ([Allende Prieto et al. 2001](#)) throughout this work. All quantities mentioned in this paper have been corrected for the gravitational magnification factors available in the literature (see references in Tab 1).

2 SAMPLE

We selected galaxies at $z > 1$, available in the literature, for which the electron temperature can be determined either from the [O III] $\lambda 1666$ or the [O III] $\lambda 4364$ auroral lines. We also required that at least one Balmer ratio be available, in order to measure the intrinsic reddening and to de-redden emission line fluxes. The only exceptions to this are

¹ It is also possible to derive direct abundances from metal recombination lines, however, these are even fainter than auroral lines, and hardly used in extragalactic studies.

Table 1. Sample used in this work. All objects are gravitationally lensed, with the exception of galaxies ID 9,10 and 11, which were broad band-selected. Redshift (z), stellar mass (M_* , in M_\odot), star formation rates (SFR, in M_\odot/yr) as derived in each of the reference works. All masses and SFR were derived using the [Chabrier 2003](#) IMF[†] or converted from [Salpeter 1955](#) IMF to [Chabrier 2003](#) (see text).

ID	Object	Reference	z	$\log_{10} M_*$	SFR
1	CSWA20	James et al. 2014	1.433	10.3	6
2	Abell860_359	Stark et al. 2014	1.702	7.60	30
3	Abell22.3	Yuan & Kewley 2009	1.703	8.5	76
4	RCSGA ¹	Rigby et al. 2011	1.704	10.0	106
5	A1689_31.1	Christensen et al. 2012a,b	1.8	7.7	1
6	SMACS_0304	Christensen et al. 2012a,b	1.963	10.57	16
7	MACS_0451	Stark et al. 2014	2.06	7.49	906
8	COSMOS_12805	Kojima et al. 2017	2.159	9.24	18
9	BX660	Erb et al. 2016	2.174	9.73	29
10	BX74	Erb et al. 2016	2.189	9.72	58
11	BX418	Erb et al. 2016	2.305	9.45	52
12	S16-stack ²	Steidel et al. 2016	2.396	9.8	29
13	COSMOS-1908	Sanders et al. 2016	3.077	9.3	49
14	Lynx arc ³	Villar-Martín et al. 2004	3.357	7.49	54
15	SMACS_2031 ⁴	Christensen et al. 2012a,b	3.5	9.16	18
16	SGAS_1050	Bayliss et al. 2014	3.625	9.5	84

¹ RCSGA_032727-132609; ² Composite spectra; ³ See also [Fosbury et al. 2003](#); ⁴ See also [Patrício et al. 2016](#).

the Lynx arc ([Fosbury et al. 2003](#); [Villar-Martín et al. 2004](#)), and SMACS2031 ([Christensen et al. 2012b](#); [Patrício et al. 2016](#)), for which lower transition Balmer lines ($H\alpha$, $H\beta$ or $H\gamma$) are not available to derive reddening. However there is evidence for very low dust content from SED fitting, so we also include these galaxies in this study. This resulted in a sample of 16 individual galaxies between $1.4 < z < 3.6$, all of them strongly lensed except three luminosity selected galaxies, plus a composite spectrum. We list all of these in Table 1.

The sample spans a stellar mass range of $7.5\text{--}10.5 \log_{10} M_\odot$ and a SFR range of a couple of solar masses per year up to almost $1000 M_\odot/\text{yr}$. Most of these masses were calculated using the [Chabrier 2003](#) initial mass function (IMF), with the exception of Abell860_359 and the Lynx arc, where the [Salpeter 1955](#) IMF was used. For these two objects, we correct the mass and SFR by dividing them by a factor of 1.8, to rescale these values to the [Chabrier 2003](#) IMF. Several stellar population models were used, with the majority of works (13/16) using the [Bruzual & Charlot 2003](#) models. The stellar mass of CSWA20 (ID 1) was not available in [James et al. 2014](#) and we calculate it from the 5-filter (ugriz) Sloan Digital Sky Survey photometry of image 1 in [Pettini et al. 2010](#). We used the SED fitting code HyperZ ([Bolzonella et al. 2000](#)) to determine the best fitting template spectra from a set of ([Bruzual & Charlot 2003](#)) models that use the [Chabrier 2003](#) initial mass function. We fixed the redshift to that of the source, and computed the scaling factor for the best fit model, from which we can determine the stellar mass. The procedure was the same as outlined in [Christensen et al. 2012a](#). We use the [James et al. 2014](#) magnification factor of $\mu=11.5$ to scale the observed magnitudes to their intrinsic (i.e. lensing corrected) values and

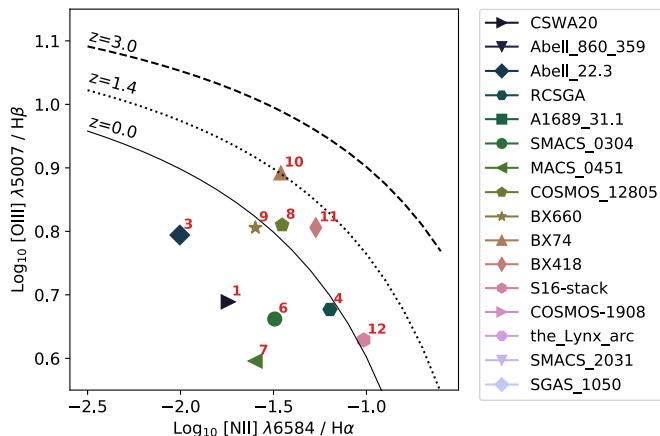


Figure 1. BPT diagram with the classification line of Kewley et al. (2013) at $z=1.4$ and $z=3.0$ in dotted and full black lines, respectively. Line ratios were calculated with extinction corrected fluxes from Table B1.

compute the total stellar mass of the galaxy to be $\log M_{\star} = 10.3 \pm 0.3 M_{\odot}$. Overall, the sample spans a wide range of masses and SFRs, suitable to test metallicity calibrators at high- z in different regimes.

None of the galaxies in the sample was identified as an AGN by previous works. We confirm this in Fig. 1 (right panel) plotting our sample in the BPT diagram ($[\text{N II}] \lambda 6585 / \text{H}\alpha$ vs $[\text{O III}] \lambda 5007 / \text{H}\beta$, Baldwin et al. 1981) and comparing it with the classification criteria of Kewley et al. 2013, that separates AGN from star-forming dominated high-redshift galaxies. All the ten galaxies with the relevant lines available are consistent with being powered by star-formation and not AGN. Galaxies with ID 2, 5, 13, 14, 15 and 16 (see Table 1) do not have the necessary lines to use this diagnostic plot, but for most galaxies other arguments can be used to rule AGN presence as unlikely. For Abell.860.359 (ID 2), Abel.31.1 (ID 5) and SMACS.2031 (ID 15), both the absence of $\text{N V } \lambda \lambda 1238, 1242$ and $\text{He II } \lambda 1640$, and the low $\text{C IV } \lambda \lambda 1548, 1550 / \text{C III}] \lambda \lambda 1907, 1909$ ratio when compared with typical narrow-line AGN values, make AGN presence not probable (Stark et al. 2014; Christensen et al. 2012b). Sanders et al. 2016 argue that the low stellar mass and lack of strong peak emission in the central region of COSMOS-1908 (ID 13) make the presence of an AGN improbable. Villar-Martín et al. claim that the Lynx arc (ID 14) emission lines ratios can be well described by models powered by star-formation and not an AGN. Finally, the SGAS_1050 (ID 16) spectrum also does not contain emission lines usually associated with AGN emission, such as N V , and also no variation in the emission line widths is found in the data (Bayliss et al. 2014), removing AGN as the most likely dominant source of ionising photons. Overall, although it is not possible to absolutely exclude the presence of AGNs in our sample, it seems that star-formation is the main ionising source in these $z \sim 2$ galaxies.

3 ELECTRON TEMPERATURE AND GAS-PHASE REDENNING

In this section, we re-derive the electron temperature and redennig corrections based on the line fluxes available in the literature. This ensures that our sample is treated homogeneously and that differences in T_e do not arise from the use of different atomic data.

Before performing any analysis, we correct the spectra for Galactic extinction, using Schlegel et al. 1998 dust map and the Fitzpatrick 1999 attenuation curve (assuming $R_V = 3.1$). We used the DUSTMAPS² PYTHON interface to recover the extinction value for each galaxy from the 2D dust map. This correction is nevertheless very small, in the order of 2% for $\text{H}\beta$ in most galaxies.

The first step to derive physical quantities from emission lines is to correct the intrinsic fluxes for dust extinction. The gas-phase redennig $E(B-V)$ can be derived comparing the theoretical values of Balmer line ratios in the absence of dust with the observed ones. To compute the theoretical values, we make use of the *getEmissivity* function in the PYNEB³ package (Luridiana et al. 2015). Balmer line ratios dependence on density is negligible for $n_e < 10^4 \text{ cm}^{-3}$, as it is the case of our sample (see for example Christensen et al. 2012a where using the $[\text{O II}] \lambda 3727, 29$ doublet electron densities of $n_e = 80\text{-}330 \text{ cm}^{-3}$ were derived). However, the ratios do depend on the electron temperature, although weakly. For this reason, we derive $E(B-V)$ and T_e iteratively. We use the reddened (i.e. observed, only corrected for magnification) fluxes to obtain a first guess on the electron temperature and density. Then, we compute the theoretical Balmer ratios in the absence of extinction for these conditions, and derive the extinction comparing these values with the observed ratios. The emission line fluxes are then dust corrected using the obtained $E(B-V)$ and the Calzetti et al. 2000 extinction law, appropriate for star-forming galaxies. We then recompute the electron temperature from these dust corrected fluxes, and check if it is compatible with the initial value assumed to calculate the theoretical Balmer ratios. If not, the initial temperature is updated with the value obtained after the dust correction and we repeat the process until the difference between the electron temperature value used to calculate the Balmer ratios and the electron temperature obtained after the correction is less than 50 K.

Electron temperature and density can be derived using adequate strong line ratios. These have to correspond to transitions from the same ion, so they do not depend on the total ion abundance. Moreover, to determine electron density, the two transitions also have to have their origin in atomic levels with very similar ionisation energies, and be mainly populated via collisional excitation (e.g. Osterbrock 1989). Collisional excitation strength depends both on the electronic density and temperature, but by selecting close energy levels the dependence on temperature is negligible. Conversely, by selecting levels with very different excitation energies, the dependence on density is minimized, and the electron temperature can be determined. The elec-

² <http://dustmaps.readthedocs.io/en/latest/index.html>

³ We use the "PyNeb_17_01" default atomic data set, only changing the $[\text{O III}]$ data set to "o_iii_coll_LAK99.dat" from Aggarwal et al. 1997, in order to include level 6 transitions.

tron density and temperature can then be calculated using the observed ratios and the adequate atomic transition probabilities (see [Shaw & Dufour 1995](#) for a description of the basic equations used in the atomic transition models). We use the `PYNEB` package ([Luridiana et al. 2015](#)) to perform these calculations.

With the emission lines available in our sample, we can derive the electron temperature using two ratios: $(\text{O III } \lambda 1661 + \text{O III } \lambda 1666) / [\text{O III } \lambda 5007]$ and $[\text{O III } \lambda 4364] / [\text{O III } \lambda 5007]$. If the two diagnostics are available, we make use of the $[\text{O III } \lambda 4364]$ ratio, since it is less sensitive to dust correction.

The electron density can be derived using ratios of strong emission lines in the optical, such as $[\text{O II } \lambda 3727] / [\text{O II } \lambda 3729]$ and $[\text{S II } \lambda 6717] / [\text{S II } \lambda 6731]$. However, $[\text{S II } \lambda 6717,31]$ is not available for most of the sample and only in seven galaxies is the $[\text{O II } \lambda 3727,29]$ doublet resolved. For this reason, we mostly derive densities using fainter UV lines, either $\text{O III } \lambda 1661$ and $\text{O III } \lambda 1666$ or $[\text{C III } \lambda 1907]$ and $[\text{C III } \lambda 1909]$ (see [Table 2](#)). The densities derived using these two ratios is known to differ up to an order of magnitude, most probably because these two ions have different ionisation energies and likely arise in environments of different densities, with $\text{O III } \lambda 1666$ tracing lower ionisation regions, that typically have lower electron densities (e.g. [James et al. 2014](#)). In order to have consistent results, and since $[\text{C III } \lambda 1907]$ and $[\text{C III } \lambda 1909]$ are only available for 4 galaxies which also have $\text{O III } \lambda 1661$ and $\text{O III } \lambda 1666$ measurements, we make exclusive use of the latter to derive densities. Whenever possible, we derive electron temperature and density at the same time, using the `getCrossTemDen` `PYNEB` function. If no density diagnostic is available, we assume a density of 100 cm^3 , appropriate for H II regions, and calculate the electron temperature⁴ using the `getTemDen` `PYNEB` function.

We estimate the uncertainties of the derived quantities – T_e , $E(B-V)$, and n_e – from Monte Carlo simulations, varying the line fluxes assuming a Gaussian distribution with σ equal to the associated uncertainties and centred in the measured fluxes. The values of electron temperature, density, reddening are shown in [Table 2](#) and correspond to the median value of the 500 Monte Carlo simulations of each galaxy. The lower and upper uncertainties correspond to the 16th and 84th percentiles of the same simulations. The dust corrected fluxes and their uncertainties are listed in [Table B1](#). Unphysical extinctions (i.e. $E(B-V) < 0$) were assumed to be zero and no correction was applied to the fluxes.

Finally, we compare the values of electron temperature derived here with the ones available in the literature, finding that they are broadly compatible within uncertainties, with mean absolute difference of $\sim 1300 \text{ K}$ and a minimum and maximum difference of 31 and 4460 K, respectively (see [Fig. 2](#)).

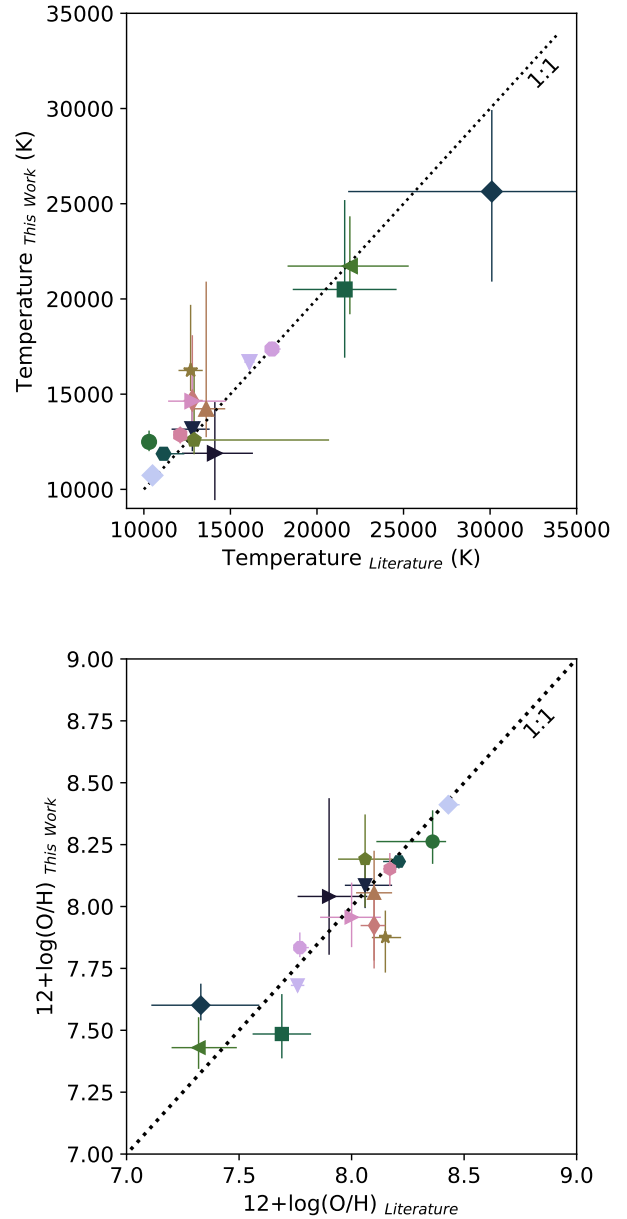


Figure 2. Comparison between electron temperature and direct metallicity from the literature and derived in this work. The 1:1 relation is plotted with a dotted line. We find a mean difference of $\sim 1300 \text{ K}$ in electron temperature between the values derived in this work and the ones from literature, and a mean difference of ~ 0.11 dex in metallicity. We use the same colours and markers as in [Fig. 1](#).

4 DIRECT METALLICITY

The total oxygen abundance can be calculated by adding the different ion abundances, that can in turn be derived if the

⁴ The electron temperature depends very weakly of the electron density, being practically constant for electron densities from 100 cm^{-3} up to 1000 cm^{-3} .

Table 2. Electron temperature, density, extinction and T_e based metallicity (see text for details). Diagnostics used for each galaxy are listed in the second column: a) $[O\text{ II}]\lambda 1661 + [O\text{ III}]\lambda 1666 / [O\text{ III}]\lambda 5007$; b) $[O\text{ III}]\lambda 4364 / [O\text{ III}]\lambda 5007$; c) $[O\text{ II}]\lambda 3727 / [O\text{ II}]\lambda 3729$; d) $[C\text{ III}]\lambda 1907 / [C\text{ III}]\lambda 1909$. Electron density for galaxies without available diagnostics was assumed to be 100 cm^{-3} . Ionic abundances and metallicity were obtained following Izotov et al. (2006) prescriptions.

Name	Diag.	T_e (K)	n_e (cm^{-3})	E(B-V) (mag.)	$12+\log(O^+/H^+)$	$12+\log(O^{2+}/H^+)$	$12+\log(O/H)_{(T_e)}$
CSWA20	b,c	11895^{+2688}_{-2459}	386^{+141}_{-104}	$0.13^{+0.08}_{-0.08}$	$7.04^{+0.54}_{-0.35}$	$7.99^{+0.39}_{-0.23}$	$8.04^{+0.40}_{-0.24}$
Abell_860_359	a,c	13160^{+1005}_{-1156}	100	$0.04^{+0.03}_{-0.03}$	$7.28^{+0.14}_{-0.09}$	$8.01^{+0.13}_{-0.09}$	$8.09^{+0.13}_{-0.09}$
Abell_22.3	a	25640^{+4280}_{-4730}	100	$0.28^{+0.26}_{-0.28}$	$7.18^{+0.38}_{-0.12}$	$7.36^{+0.17}_{-0.10}$	$7.60^{+0.09}_{-0.06}$
RCSGA	b	≤ 11870	100	$0.24^{+0.11}_{-0.07}$	≥ 7.74	≥ 7.98	≥ 8.18
A1689_31.1	b,c	20498^{+4695}_{-3583}	234^{+207}_{-139}	$0.29^{+0.30}_{-0.29}$	$6.73^{+0.13}_{-0.03}$	$7.41^{+0.18}_{-0.16}$	$7.48^{+0.16}_{-0.10}$
SMACS_0304	a,c	12493^{+392}_{-486}	1292^{+3938}_{-1013}	$0.21^{+0.03}_{-0.01}$	$7.86^{+0.24}_{-0.12}$	$8.02^{+0.08}_{-0.07}$	$8.26^{+0.13}_{-0.09}$
MACS_0451	b	21725^{+2613}_{-2529}	100	$0.00^{+0.03}_{-0.00}$	$6.70^{+0.07}_{-0.05}$	$7.34^{+0.14}_{-0.11}$	$7.43^{+0.12}_{-0.09}$
COSMOS_12805	a	12592^{+3785}_{-751}	100	$0.00^{+0.27}_{-0.00}$	$7.67^{+0.18}_{-0.17}$	$8.03^{+0.17}_{-0.20}$	$8.19^{+0.18}_{-0.19}$
BX660	a	16244^{+3446}_{-1076}	100	$0.00^{+0.17}_{-0.00}$	$6.91^{+0.10}_{-0.09}$	$7.83^{+0.11}_{-0.15}$	$7.87^{+0.11}_{-0.14}$
BX74	a	14231^{+6678}_{-1490}	100	$0.10^{+0.26}_{-0.10}$	$7.13^{+0.18}_{-0.18}$	$8.00^{+0.17}_{-0.28}$	$8.06^{+0.17}_{-0.27}$
BX418	a	14667^{+3427}_{-1212}	100	$0.00^{+0.19}_{-0.00}$	$7.00^{+0.14}_{-0.13}$	$7.87^{+0.17}_{-0.17}$	$7.92^{+0.16}_{-0.17}$
S16-stack	a,c	12861^{+433}_{-453}	496^{+154}_{-142}	$0.21^{+0.06}_{-0.02}$	$7.74^{+0.06}_{-0.07}$	$7.94^{+0.06}_{-0.07}$	$8.15^{+0.06}_{-0.07}$
COSMOS_1908	b,c	14633^{+1757}_{-1655}	714^{+764}_{-436}	$0.09^{+0.29}_{-0.09}$	$6.82^{+0.14}_{-0.12}$	$7.92^{+0.14}_{-0.12}$	$7.96^{+0.14}_{-0.12}$
Lynx arc	a,d	17369^{+390}_{-345}	16014^{+27546}_{-10973}	0	$6.82^{+0.33}_{-0.23}$	$7.79^{+0.03}_{-0.03}$	$7.83^{+0.06}_{-0.04}$
SMACS_2031	a,c	16684^{+387}_{-346}	525^{+308}_{-269}	0	$6.83^{+0.05}_{-0.05}$	$7.62^{+0.02}_{-0.02}$	$7.68^{+0.03}_{-0.02}$
SGAS_1050	a,c	10735^{+259}_{-295}	615^{+597}_{-346}	0	$7.42^{+0.06}_{-0.06}$	$8.37^{+0.04}_{-0.03}$	$8.41^{+0.04}_{-0.03}$

electron temperature and density are known. Usually, only O^+/H^+ and O^{2+}/H^+ are accounted for, since higher ionisation states typically contribute to less than 1% to the total abundances (Izotov et al. 2006). To calculate O^+/H^+ and O^{2+}/H^+ abundances we use the *getIonAbundance* function of PYNEB. This function assumes that the system is in equilibrium, i.e. the number of excitations and de-excitations is the same, and calculates the density of the ion relative to hydrogen based on the atomic transition probabilities, the atomic level populations (set by the electron density and temperature calculated in the previous section) and the observed line ratios (see Luridiana et al. 2015 for details).

To determine O^{2+}/H^+ , we use the derived electron temperatures and densities, and the extinction corrected fluxes of $[O\text{ III}]\lambda 4364$ and $[O\text{ III}]\lambda 5007$. The O^+ ion is formed in regions with lower electron temperature than O^{2+} , and we calculate the appropriate electron density for the O^+/H^+ ratio using Izotov et al. 2006 equation 14 for low metallicities:

$$t(\text{OII}) = -0.577 + t(\text{OIII}) \times (2.065 - 0.498 t(\text{OIII})) \quad (1)$$

with $t(\text{OII}) = 10^{-4}T(\text{OII})$ and $t(\text{OIII}) = 10^{-4}T(\text{OIII})$, and where $T(\text{OIII})$ is the temperature derived from $[O\text{ III}]\lambda 4364$, used to calculate the O^{2+}/H^+ ion abundance, and $T(\text{OII})$ the inferred temperature of O^+ . The O^+/H^+ abundance is then estimated using $T(\text{OII})$ and again the *getIonAbundance* function with extinction corrected fluxes of $[O\text{ II}]\lambda 3727$ and $[O\text{ II}]\lambda 3729$. The total oxygen abundance is calculated by adding these two ion abundances. As before, errors are derived following a Monte Carlo technique, taking into account emission line fluxes, T_e and n_e uncertainties. The results are listed in Table 2 and compared with literature direct metallicities in Fig. 2. We find a good agreement between the metallicity derived here and the literature values, with a mean difference of 0.11 dex (maximum of 0.27 dex and min-

imum of 0.01 dex), and without systematic differences with metallicity.

5 COMPARISON WITH COMMONLY USED EMPIRICAL CALIBRATIONS

In this section, we compare the metallicities derived using the direct method with the results obtained using common strong line diagnostics, calculated using the extinction corrected fluxes listed in Table B1. We examine strong line calibrations that make use of the following line ratios:

$$\begin{aligned} \mathbf{R23} & ([O\text{ II}]\lambda 3727,29 + [O\text{ III}]\lambda 4959 + [O\text{ III}]\lambda 5007) / H\beta \\ \mathbf{O3} & [O\text{ III}]\lambda 5007 / H\beta \\ \mathbf{O2} & [O\text{ II}]\lambda 3727,29 / H\beta \\ \mathbf{O32} & [O\text{ II}]\lambda 3727,29 / [O\text{ III}]\lambda 5007 \\ \mathbf{O3N2} & ([O\text{ III}]\lambda 5007 / H\beta) / ([N\text{ II}]\lambda 6585 / H\alpha) \\ \mathbf{N2} & [N\text{ II}]\lambda 6585 / H\alpha \\ \mathbf{Ne3O2} & \text{Ne III } \lambda 3869 / [O\text{ II}]\lambda 3727,29 \end{aligned}$$

For each diagnostic, we calculate the metallicities applying the calibrations from Maiolino et al. 2008, Curti et al. 2017, Jones et al. 2015 and Bian et al. 2018 (hereafter M08, C17, J15 and BKD18), whenever available. Most calibrations are in the form of $\log_{10} R = \sum_n c_n x^n$, where R is the line ratio, c_n the calibration coefficients and x^n the metallicity in $12+\log(O/H) - 8.69$. The higher polynomial degree n varies from 1 to 4, depending on the line ratio and calibration used. We compile all the calibrations and list them in four tables in Appendix A. For each lines ratio value, we numerically find the metallicity that minimises the distance between the observed ratio and the one predicted by the appropriate strong line calibration ($\log_{10} R_{obs} - \log_{10} R$), using the PYTHON package LMFIT (Newville et al. 2014). The only exceptions are some calibrations of BKD18 ($N2, O3N2, O32$ and $Ne3O2$), which are in the form $x = c_0 + c_1 \log_{10} R$, and for

which the metallicity can be derived directly without minimisation. We again use Monte Carlo simulations (varying line fluxes) to obtain the metallicity and upper and lower uncertainties. We do not include the intrinsic dispersion of the calibrations available both for [Curti et al. 2017](#) and [Jones et al. 2015](#) in our calculations of metallicity uncertainties, since we also wish to compare the dispersion obtained at $z \sim 2$ with the one derived at lower redshifts.

To study the accuracy and precision of the strong line methods at $z \sim 2$, we compute the difference between the metallicity derived using the strong line calibrations and the metallicity derived via the direct method (Sect. 4) and calculate both the mean (\bar{x}) and the standard deviation (σ) of the residuals. To test how sensitive these results are to our particular data set, since our sample is small, we utilise a bootstrapping technique, drawing 500 random samples with replacement of the available galaxies for each diagnostic. We describe the details of this process for each set of calibrations in the subsections below.

5.1 [Maiolino et al. 2008](#) (M08)

M08 derive metallicity calibrations for the $R23$, $O3$, $O2$, $N2$, $O3N2$ and $Ne3O2$ ratios, using Sloan Digital Sky Survey (DR3 and DR4) galaxies. Note that in M08 $O3N2$ is the ratio between $[O\text{III}]\lambda 5007/[N\text{II}]\lambda 6585$, slightly different from the one used in other works and cited in the previous subsection. For the low metallicity range, the metallicities were derived using the direct method, while for the high metallicity range photoionisation models were utilised. These data extend from 7.0 up to 9.2 in $12+\log(O/H)$ and the calibrations were derived within this range (see M08 figure 5). Some of these ratios – $R23$, $O3$ and $O2$ – are degenerate, with a high and low metallicity solution for each ratio value. If the direct method is not available, as it is almost always the case at high- z , the correct solution can be chosen, for example, based on the metallicity yield by non-degenerate calibrations: $O23$, $O3N2$, $N2$ or $Ne3O2$. Alternatively, the mass-metallicity relation can also be used to choose the most likely metallicity solution.

When determining the metallicity of an object, all the available line ratios of the same set of calibrations should be used simultaneously, as done for example in M08, but since we aim at testing the accuracy of individual diagnostics applied to higher redshift galaxies we derive metallicities using each diagnostic independently. This means that we have to choose between one of the metallicity solutions when dealing with the three degenerate ratios. In our sample, the $O32$ diagnostic is available for all objects, so it can be used for this purpose. Although this is certainly not the case for all high- z objects, we prefer to use this prior knowledge of the expected metallicity in order to reject the wrong metallicity branch, since our aim is to verify what is the accuracy of these diagnostics at $z \sim 2$, and choosing the wrong branch would artificially increase the residuals.

For all diagnostics, we allow the solutions to vary between $12+\log(O/H) = 7$ and 9, the range of validity of the M08 calibrations (based on their fig. 5). For each of the Monte Carlo simulations, we randomly pick the initial guess for the metallicity within this range. For the degenerate ratios however, the initial guess of the metallicity is based on the previously calculated $O32$ metallicity, which drives the

solution towards the correct metallicity branch, although the allowed range of solutions still spans 7-9 in $12+\log(O/H)$. We obtained similar results when using direct method metallicity as the initial guess, instead of the $O32$ metallicity.

The $R23$, $O3$ and $O2$ diagnostics present yet another issue: since they reach a local maximum in the middle of the considered metallicity range, there is a maximum value of the line ratio for which the calibrations can be used (the other, more linear, diagnostics also have maximum valid values of $\log R$, but they are less problematic since they roughly correspond to the minimum or maximum of allowed metallicity). $R23$ reaches its maximum at $12+\log(O/H)=8.050$ for $\log(R23)=0.938$, $O3$ at 7.894 for $\log(O3)=0.746$ and $O2$ at 8.702 for $\log(O2)=0.5606$. In our sample of 16 galaxies, 10 have $R23$ ratios higher to 0.938 (see Table B2), although, including uncertainties, this number reduces to 4 (ID 4,13,14,16). We notice that this is perfectly natural, since the fit done to obtain the strong line calibrations minimises the distance to all data points, some galaxies will have ratios above the fit maximum (see M08 figure 5), and could possibly be solved by including the fit uncertainties. However, since these are not reported in M08, we avoid estimating metallicities outside of the validity range, we reject the 4 galaxies mentioned above and, for the remaining 6 problematic ones, we reject Monte Carlo simulations where the ratio is above the maximum of the calibration. For the $O3$ diagnostic, accounting for uncertainties, only 3 galaxies have ratios that are higher than 0.746, and all galaxies have $O2$ ratios lower than the maximum (see Table B2).

Finally, we plot the results and compare them with the metallicities derived using the direct method in Fig. 3 and show the number of galaxies used in each comparison and mean and standard deviations (and respective uncertainties obtained using a bootstrapping technique) in Table B3.

5.2 [Jones et al. 2015](#) (J15)

These calibrations were derived with a set of $z \sim 0.8$ galaxies from the DEEP2 Galaxy Redshift Survey with available auroral lines. The authors derive calibrations for $R23$, $O2$, $O3$, $O32$, $Ne3O2$ and $Ne3O3$ with data that spans metallicities from 7.6 up to 9.0 in $12+\log(O/H)$. Comparing these calibrations with the ones obtained from local samples, J15 see no evolution with redshift, up to $z = 0.8$. As in the M08 calibrations, $R23$, $O2$ and $O3$ are degenerate and with maxima of $12+\log(O/H)=7.919$ at $\log(R23)=0.967$, $12+\log(O/H)=7.845$ at $\log(O3)=0.814$ and $12+\log(O/H)=8.420$ at $\log(O2)=0.561$. We apply the same procedure here as for the M08 calibrations, searching for solutions within $7.6 < 12+\log(O/H) < 9.0$. The $Ne3O3$ diagnostic is extremely degenerate, with less than 0.2 dex variation in the line ratio for metallicities between $12+\log(O/H)=7.6$ and 9.0, and we do not include it in the global comparison.

We look for solutions between 7.6 and 8.6 in $12+\log(O/H)$ for all calibrations except for $O3$, where the upper limit is set to 9.0, following J15 figure 9. The results are plotted in Fig. 4 and shown in Table B3.

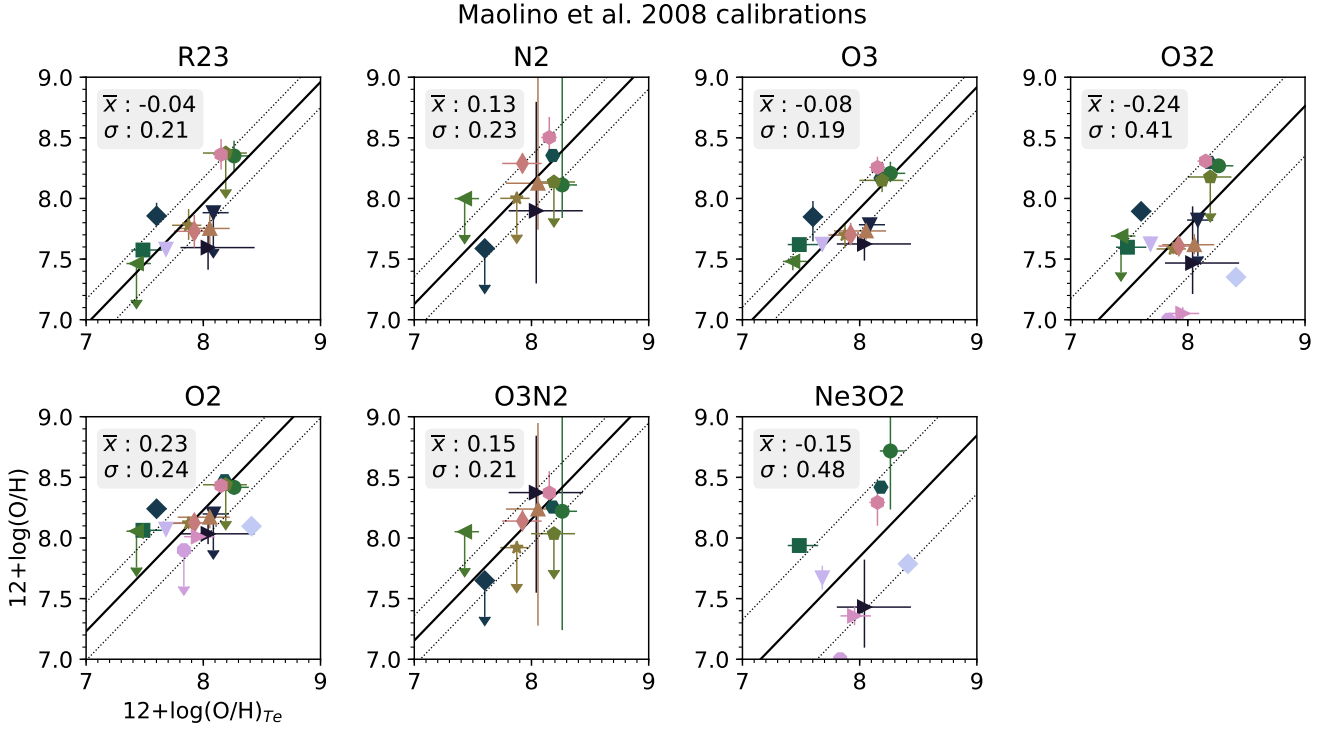


Figure 3. Comparison between metallicities derived using the [Maolino et al. \(2008\)](#) calibrations (vertical axis) and the direct method (horizontal axis). Vertical uncertainties with arrows depict upper limits (where no uncertainties were available for one of the line fluxes). The mean and standard deviation of the residuals of the difference between these two values are shown in the upper left of each plot and are plotted in thick and dashed black lines, respectively. Objects have the same colours and markers as in Fig. 2.

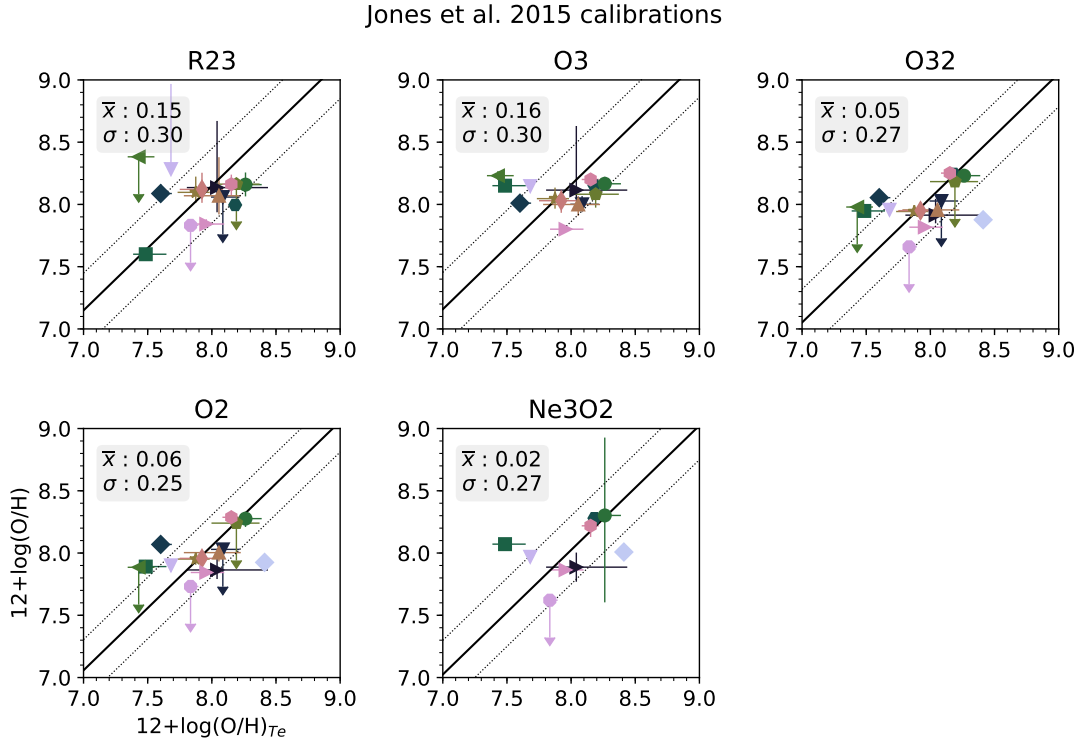


Figure 4. Comparison between metallicities derived using the [Jones et al. \(2015\)](#) calibrations and the direct method. See Fig. 3 for details.

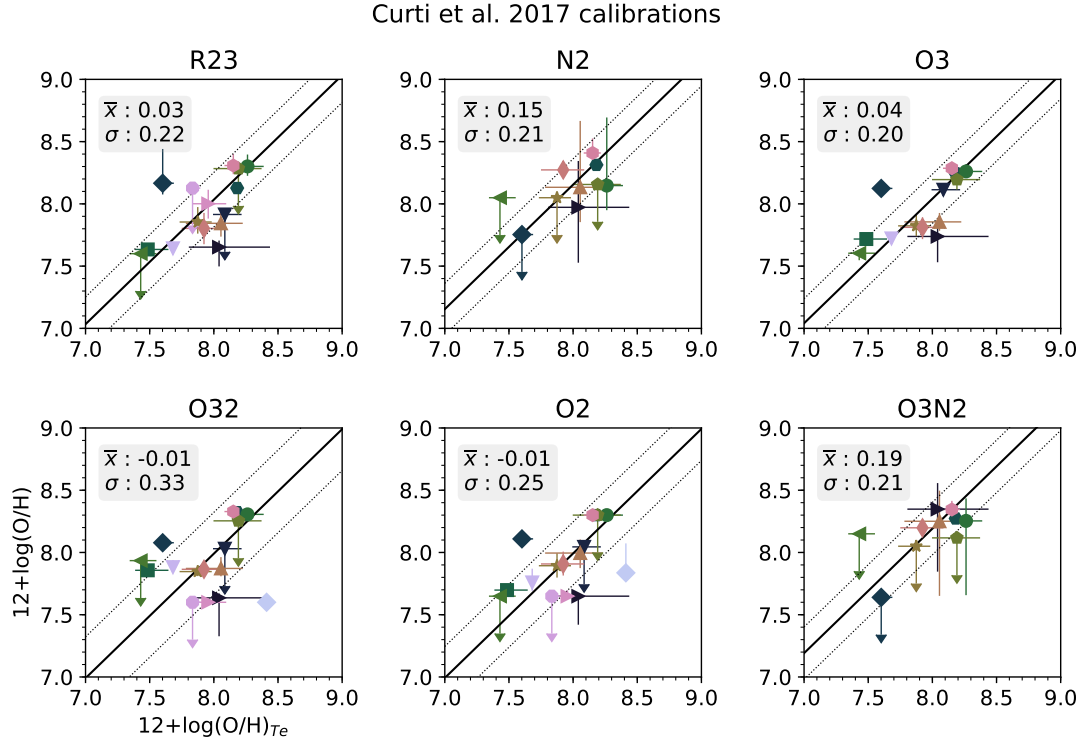


Figure 5. Comparison between metallicities derived using the Curti et al. (2017) calibrations and the direct method. See Fig. 3 for details.

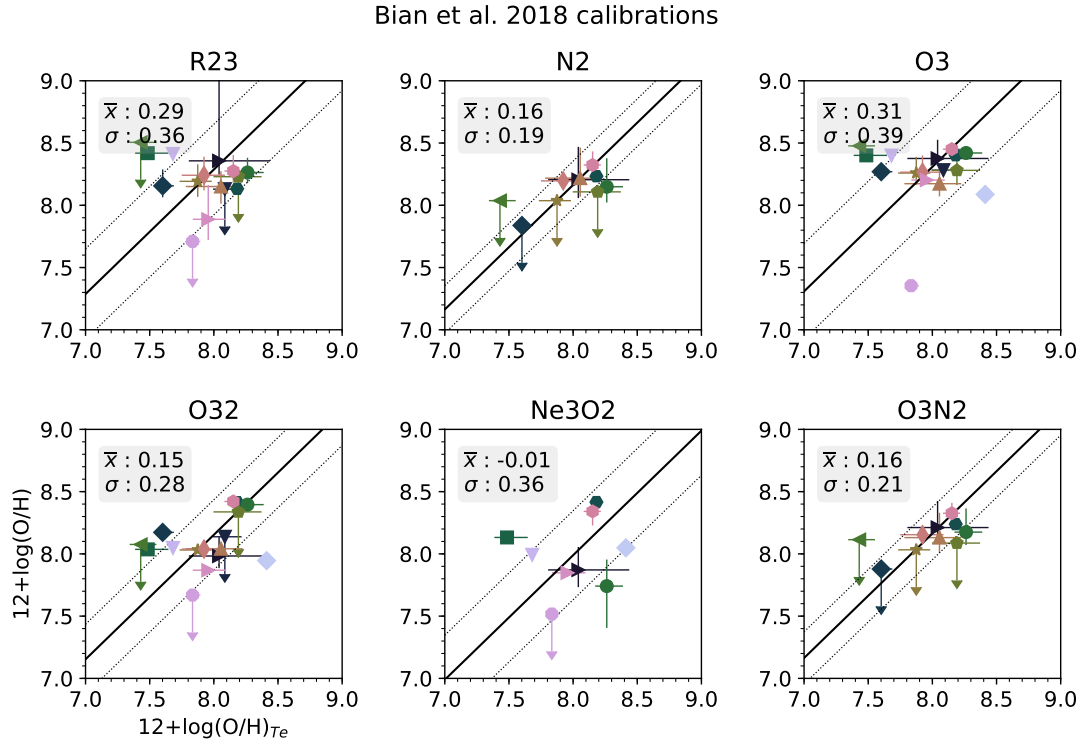


Figure 6. Comparison between metallicities derived using the Bian et al. (2018) calibrations and the direct method. See Fig. 3 for details.

5.3 Curti et al. 2017 (C17)

These are fully empirical calibrations derived from a sample of 110000 Sloan Digital Sky Survey (DR7) galaxies. The authors stack galaxies accordingly to their strong line ratios in order to increase the signal to noise of the spectra, allowing robust detections of oxygen auroral lines, even in the highest metallicity ranges. C17 provide calibrations for the $R23$, $N2$, $O3$ ($R3$, in C17 nomenclature), $O2$ ($R2$), $O32$ and $O3N2$ diagnostics, and the metallicity ranges in which they can be applied, usually $7.6 < 12 + \log(O/H) < 8.85$ (see C17 table 2). As in the previous calibrations, $R23$, $O2$ and $O3$ are degenerate, although to a lesser extent, since the applicability range of these calibrations is more restricted. Indeed, $R23$ and $O3$ minimum valid metallicity is 8.4 and 8.3 in $12 + \log(O/H)$, respectively. Within our sample, only one galaxy (SGAS_1050, ID 16) has metallicity ≥ 8.3 $12 + \log(O/H)$, so in principle we should not be able to use these two diagnostics. Nevertheless, we still test $R23$ and $O3$ C17 calibrations, allowing the minimum metallicity to go down to 7.6 as the other diagnostics in C17, although we warn the reader that this is outside the applicability range given by C17. We calculate the metallicities following the same procedure detailed in the previous section and present the results in Fig. 5.

5.4 Bian et al. 2018 (BKD18)

Similarly to C17, this work also uses SDSS (DR7) stacked data to derive new metallicity calibrations from direct metallicity measurements. The main difference is the selection criteria of the stacked galaxies. The authors select 443 local galaxies that occupy the same BPT region as the $z \sim 2.3$ star-forming galaxies analysed in Steidel et al. 2014. This sample of local $z \sim 2$ analogs is then stacked based on their $[N\ II] \lambda 6585/H\alpha$ ratios, producing 7 stacked spectra in which the $[O\ III] \lambda 4364$ line can be detected and used to calculate the direct metallicity.

BKD18 derive calibrations for $R23$, $N2$, $O3$, $O32$ and $O3N2$ diagnostics. Only $R23$ and $O3$ are degenerate with local maxima at $12 + \log(O/H) = 7.87$ and $\log_{10}(R23) = 0.99$ and $12 + \log(O/H) = 7.77$ and $\log_{10}(O3) = 0.98$, respectively. Only SGAS_1050 has an $R23$ ratio higher than this local maximum and all galaxies have $O3$ ratios lower than 0.98.

The stacked spectra have metallicities between $7.8 < 12 + \log(O/H) < 8.4$, and does not extend in metallicity range to include the 3 lowest metallicity galaxies in our sample (see Table 2). Nevertheless, as for the previous calibrations, we also include these galaxies in the sample, allowing the metallicity solutions to be as low as 7 in $12 + \log(O/H)$. The comparison between the metallicities obtained with the BKD18 calibrations and the direct metallicities is shown in Fig 6.

5.5 Strong line methods at $z \sim 2$

We summarise our results in Figure 7, presenting the mean and standard deviation of the residuals between the metallicity derived using each diagnostic and calibration and the direct method.

We first analyse the accuracy and precision at $z \sim 2$ of the different diagnostics within the same calibration set.

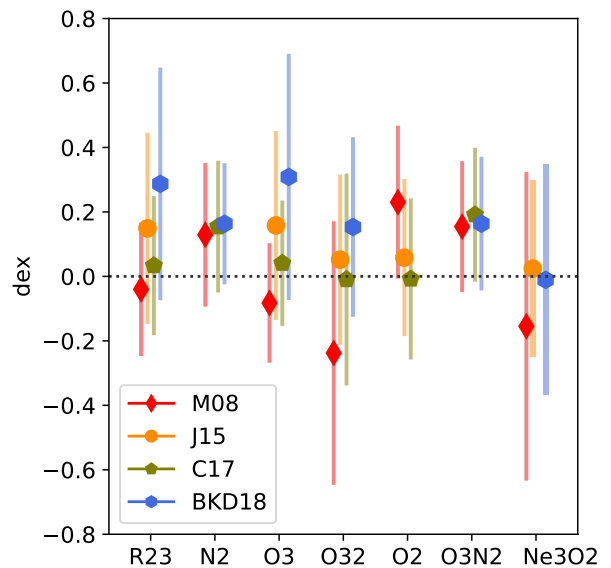


Figure 7. Summary of the accuracy and precision of the 7 strong line ratios tested here (in the horizontal axis) for the different empirical calibrations tested here (M08, J15, C17 and BKD18, in red, orange, green and blue, respectively). The mean difference between each ratio and the direct metallicity (\bar{x}) is given by the markers, and the standard deviation of the residuals ($\sigma_{z \sim 2}$) is given by the vertical bars. Error bars on both quantities can be found in Table B3.

For each diagnostic, we use the mean and the standard deviation of the residuals between the metallicity obtained using strong lines methods and the one derived using the T_e method (that we take to be the true metallicity). All values can be found in Table B3.

For M08, the lowest residuals are found for $R23$, with mean residuals of -0.04 ± 0.06 dex. The second most accurate diagnostic is $O3$, under-predicting the metallicity only by -0.08 ± 0.06 dex, when compared with the direct method. The worst accuracy is obtained with $O32$ and $O2$, with mean residuals of -0.24 ± 0.11 and 0.23 ± 0.06 dex, respectively. Most diagnostics have a precision (dispersion in the residuals) of about 0.2 dex, with the exceptions of $O32$ and $Ne3O2$, that have residual $\sigma_{z \sim 2}$ around 0.4 dex. J15 calibrations, the only ones tested here that were calibrated also using non-local galaxies (up to $z \sim 0.8$), show an overall good agreement with the direct metallicities, with a maximum mean residual of ~ 0.15 dex for $R23$ and $O3$, and the remaining diagnostics with $\bar{x} \leq 0.06$ dex. The dispersion in the residuals of J15 are slightly higher than for M08 and C17, with $\sigma_{z \sim 2}$ around 0.3 dex. Using C17 calibrations, the lowest mean residuals are found using the $R23$, $O2$ and $O32$ diagnostics, even when utilised outside their applicability range. The dispersions are comparable to M08, varying between 0.21 and 0.33 dex. Finally, the $Ne3O2$ diagnostic has a low mean residual in the BKD18 diagnostics ($\bar{x} = -0.01 \pm 0.11$), although this value is higher for other diagnostics, typically at about 0.16 dex, but as high as 0.3 dex for $R23$ and $O3$. The precision of these

calibrations is also usually lower, with $\sigma_{z \sim 2}$ typically around 0.3 dex and never lower than 0.19 dex, but comparable to the other calibrations tested.

Perhaps unsurprisingly, the dispersion at $z \sim 2$ is higher than the dispersion found both by J15 and C17 (calculated from data that is mostly comprised by low redshift objects). For J15, the typical dispersion is ~ 0.28 dex for high- z , while it varies between 0.06 and 0.23 dex for their studied sample. For C17 calibrations, we obtained dispersions between 0.2 and 0.3 dex, where in the local sample used to derive these calibrations this value varies between 0.07 and 0.26 dex.

We find that no single line ratio systematically outperforms the others, neither does one set of calibrations. The $R23$ and $O3$ diagnostics in the M08 and C17 calibrations have both a good accuracy, with mean residuals very close or compatible with zero, and a good precision, with dispersions of about 0.2 dex. The $O2$ ratio also yields low mean residuals with the J15 and C17 calibrations, but has a higher dispersion (0.25 dex) than $R23$ and $O3$. $N2$ and $O3N2$ are systematically offset in all calibrations, generally predicting higher metallicities than the ones measured using the direct method. Since both diagnostics include nitrogen, this might possibly indicate an evolution of the nitrogen abundance relative to oxygen with cosmic time, although our analysis and sample size is not suited to study this evolution. Finally, both $O32$ and $Ne3O2$ have large dispersions with all calibrations, varying between 0.27 to 0.48 dex, which might result in metallicities off by a factor of ~ 2 -4 when applying these diagnostics at $z \sim 2$. These calibrations primarily depend on the ionisation parameter, their dependence on metallicity is mostly an indirect consequence of a correlation between metallicity and ionisation parameter in most galaxies (Kewley & Dopita 2002). It is therefore not surprising that the dispersion obtained with these diagnostics is higher than with those directly depending on metallicity.

We remind nevertheless that these results were obtained with a small sample, from 16 objects $O32$ and $O2$ but as low as 9 for $Ne3O2$, and a higher number of objects would be desirable to establish these results more robustly. Furthermore, we also probe a restricted metallicity range ~ 7.4 -8.4 $12+\log(O/H)$ (see Fig. 2), that does not fully cover the high metallicity part of M08 and J15 calibrations, that used data up to ~ 9 $12+\log(O/H)$, where, for example the $N2$ diagnostic is likely to become problematic. In the case of C17 calibration, the metallicity range probed here is close to the applicability range given by the authors ($7.6 < 12+\log(O/H) < 8.85$, see their table 2), so this is less of an issue. However, most objects of our sample have metallicities between 8 and 8.5 in $12+\log(O/H)$, so it would be important to increase the number of low and high metallicity galaxies in this study in order to increase the robustness of these results, and to possibly look for trends in the residuals with metallicity.

6 COMPARISON WITH PÉREZ-MONTERO ET AL. 2014 CALIBRATIONS

Contrary to the previous calibrations, mostly empirical, Pérez-Montero 2014 (hereafter PM14) provide a set of fully theoretical calibrations. The authors provide a grid of photoionisation models, obtained using CLOUDY (Ferland et al.

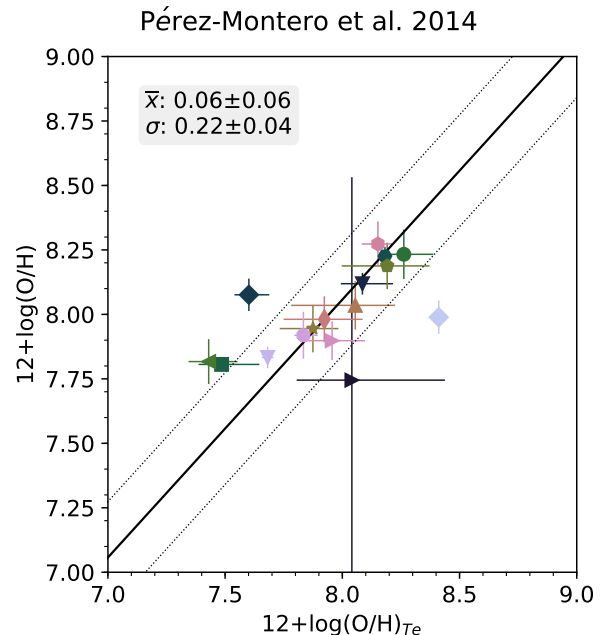


Figure 8. Comparison between metallicity derived using the Pérez-Montero 2014 calibrations (including all strong emission lines available, but not $[O\text{ III}]\lambda 4364$) and the direct method. The same markers and colours as in Fig. 3 are used here.

2013) to calculate emergent spectra. The grid spans a large range of O/H ($7.1 < 12+\log(O/H) < 9.1$) and N/O abundances ($0 < \log(N/O) < -2$) as well as ionisation parameters ($-4 < \log(U) < -1$). PM14 also provides a PYTHON implementation of their procedure, HII-CHI-MISTRY⁵, that determines the best grid model for a given set of emission lines. Unlike the previously tested calibrations, this method makes use of all the emission ratios at the same time, finding the best model in the grid taking into account all line fluxes.

PM14 test their method using a large sample of local objects where auroral lines are detected. When all the emission lines are utilised – $[O\text{ II}]\lambda 3727, 29$, $[O\text{ III}]\lambda 4364$, $[O\text{ III}]\lambda 5007$, $[N\text{ II}]\lambda 6585$, $[S\text{ II}]\lambda 6717, 6731$ and $H\beta$ – they find a dispersion of 0.07 dex for $12+\log(O/H) < 8.0$ and 0.14 dex for $12+\log(O/H) > 8.0$ of their solutions when compared with the direct method. PM14 also test the scenario where the $[O\text{ III}]\lambda 4364$ line is not detected, usually the case at high metallicity and at high- z due to the faintness of the auroral line. They find that this yields poor results when all models in the grid are included, but limiting the search to a sub-sample of models in the grid determined in P14 (shown their figure 3), a much better agreement is obtained. When the $[O\text{ III}]\lambda 4364$ line is not available, and using the set of empirically limited grids in $\log U$ (ionisation parameter), a dispersion of 0.16 dex for the low metallicity objects ($12+\log(O/H) < 8.0$) and 0.05 dex at higher metallicities is found. If besides $[O\text{ III}]\lambda 4364$, the $[N\text{ II}]\lambda 6585$ line is not available, a set of $\log(N/O)$ empirically limited grids can be used, and a global dispersion of 0.19 dex is reached in the

⁵ <http://www.iaa.es/~epm/HII-CHI-mistry.html>

local sample (although with an overestimation of 0.26 dex of the oxygen abundances for $12+\log(\text{O}/\text{H}) < 8.0$ objects).

We investigate the results obtained with the PM14 method using all the strong emission lines available for each galaxy, but not the $[\text{O III}] \lambda 4364$ emission line. In this case, the procedure automatically selects the empirically limited grids to be used. We use version 3 of HII-CHI-MISTRY with interpolated grids, with a resolution of 0.02 dex for $12+\log(\text{O}/\text{H})$ and 0.025 dex for $\log(\text{N}/\text{O})$, for all tests. The results and comparison with the $z \sim 2$ sample are shown in Fig. 8.

The results obtained have low mean residuals ($\bar{x} = 0.06 \pm 0.05$ dex) and also a reasonable low dispersion ($\sigma = 0.22 \pm 0.04$), which is comparable to the best empirical calibrated diagnostics (e.g. $R23$ with the M08 and J15 calibrations or $O32$ with the C17 results).

7 SUMMARY AND CONCLUSIONS

We gathered a sample of 16 high- z galaxies from $z \sim 1.4$ up to $z \sim 3.6$ where auroral lines are detected, with the aim of testing the accuracy and precision of the metallicity derived using strong line methods at $z \sim 2$. Using line fluxes from literature, we homogeneously re-derive the oxygen abundances through the direct method, which relies on the determination of the electron temperature from auroral line ratios, and is considered the most accurate method available.

We compare the direct metallicities to the metallicities derived using the strong line ratios $R23$, $O32$, $O3$, $O2$, $N2$, and $Ne3O2$. To do so, we test four different calibration sets from Maiolino et al. 2008, Jones et al. 2015, Curti et al. 2017 and Bian et al. 2018. Since some of these commonly used diagnostics ($R23$, $O3$ and $O2$) are degenerate, this is, for the same ratio value there are two possible metallicity solutions, some a priori knowledge about the metallicity is needed in order to choose the correct branch. Here, we base our choice in the results obtained with $O32$. Moreover, these degenerate diagnostics have a local maximum in the metallicity range considered, so there is also a maximum ratio for which the calibrations can be formally applied. In our sample of 16 galaxies, 10 presented $R23$ ratios higher than this allowed maximum. This may bring some extra uncertainty when using the $R23$ ratio to derive metallicities close to $12+\log(\text{O}/\text{H})=8.0$.

We did not find a line ratio that delivered better results irrespectively of the calibration used, neither a calibration set that outperformed the others in all diagnostics. However, there are some combinations that deliver better results, which have both low mean residuals and dispersion. We summarise these results below:

- $R23$ and $O3$ with the M08 and C17 calibration have both mean residuals very close or compatible with zero, and small dispersions (~ 0.2 dex);
- $O2$ with the J15 and C17 calibrations has comparable low mean residuals (0.06 and -0.01 dex, respectively), although a slightly higher dispersion (~ 0.25 dex);
- $N2$ and $O3N2$ have high and positive mean residuals with all the calibrations tested. This might be due to an evolution with redshift of the abundance of nitrogen relative to oxygen;
- $O32$ and $Ne3O2$ have large dispersions with all calibrations, varying between 0.27 to 0.48 dex. Since these diag-

nostics are primarily dependent on the ionisation parameter, this variability is somehow expected;

- The theoretical calibration of Pérez-Montero 2014 achieve comparable results to the best line ratios diagnostics using all available bright emission lines.

There are some caveats in this study. First, the number of galaxies at high- z for which the auroral line is detected is still small, and a bigger sample should be analysed in order to robustly confirm our results. Moreover, although we cover metallicities as low as $12+\log(\text{O}/\text{H}) = 7.4$, the higher metallicity regime, $12+\log(\text{O}/\text{H}) > 8.4$, was not tested in this study, which might be an issue when considering the most luminous, massive, and hence more metal rich, galaxies. However, the metallicity range examined in this work mostly covers the regime of $z \sim 2$ main sequence galaxies that currently have metallicity estimates. As an example, the highest metallicity of the MOSDEF Survey sample of 87 star-forming galaxies is about 8.7 in $12+\log(\text{O}/\text{H})$ (Sanders et al. 2015), approximately the same as the smaller sample of $z \sim 2.2$ galaxies in Maiolino et al. 2008. Therefore, we find that the mass and metallicity range covered in this work is adequate to confirm that most strong line methods can still be applied with reasonable confidence at $z \sim 2$. We plan to increase the sample size and expand the mass regime of galaxies at $z \sim 2$ with auroral line detections in order to confirm these results. This will also allow to explore for the first time the mass-metallicity at $z \sim 2$ employing direct metallicity estimations only, that do not depend on the local calibrations.

ACKNOWLEDGEMENTS

We thank Michael Maseda and Charles Steinhardt for useful comments about high- z flux measurements and statistics. We also thank the anonymous referee for providing useful comments that improved this work.

VP, LC, RC and HR are supported by the grant DFF - 4090-00079. This research made use of ASTROPY, a community-developed core Python package for Astronomy Astropy Collaboration et al. 2013. This research has made use of NASA's Astrophysics Data System.

The full analysis presented in this paper is available in <https://github.com/VeraPatricio/MetCalibration.git>.

REFERENCES

- Aggarwal K. M., Hibbert A., Keenan F. P., 1997, The Astrophysical Journal Supplement Series, 108, 393
- Allende Prieto C., Lambert D. L., Asplund M., 2001, *ApJ*, 556, L63
- Astropy Collaboration et al., 2013, *A&A*, 558, A33
- Baldwin J. A., Phillips M. M., Terlevich R., 1981, *PASP*, 93, 5
- Bayliss M. B., Rigby J. R., Sharon K., Wuyts E., Florian M., Gladders M. D., Johnson T., Oguri M., 2014, *ApJ*, 790, 144
- Bian F., Kewley L. J., Dopita M. A., 2018, preprint, [p. arXiv:1805.08224](https://arxiv.org/abs/1805.08224) ([arXiv:1805.08224](https://arxiv.org/abs/1805.08224))
- Bolzonella M., Miralles J.-M., Pelló R., 2000, *A&A*, 363, 476
- Bruzual G., Charlot S., 2003, *MNRAS*, 344, 1000
- Calzetti D., Armus L., Bohlin R. C., Kinney A. L., Koornneef J., Storchi-Bergmann T., 2000, *ApJ*, 533, 682
- Chabrier G., 2003, *PASP*, 115, 763

- Christensen L., et al., 2012a, *MNRAS*, **427**, 1953
 Christensen L., et al., 2012b, *MNRAS*, **427**, 1973
 Curti M., Cresci G., Mannucci F., Marconi A., Maiolino R., Esposito S., 2017, *MNRAS*, **465**, 1384
 Dessauges-Zavadsky M., D’Odorico S., Schaerer D., Modigliani A., Tapken C., Vernet J., 2010, *A&A*, **510**, A26
 Erb D. K., Pettini M., Steidel C. C., Strom A. L., Rudie G. C., Trainor R. F., Shapley A. E., Reddy N. A., 2016, *ApJ*, **830**, 52
 Ferland G. J., et al., 2013, *Rev. Mex. Astron. Astrofis.*, **49**, 137
 Fitzpatrick E. L., 1999, *PASP*, **111**, 63
 Fosbury R. A. E., et al., 2003, *ApJ*, **596**, 797
 Izotov Y. I., Stasińska G., Meynet G., Guseva N. G., Thuan T. X., 2006, *A&A*, **448**, 955
 James B. L., Aloisi A., Heckman T., Sohn S. T., Wolfe M. A., 2014, *ApJ*, **795**, 109
 Jones T., Martin C., Cooper M. C., 2015, *ApJ*, **813**, 126
 Kewley L. J., Dopita M. A., 2002, *ApJS*, **142**, 35
 Kewley L. J., Ellison S. L., 2008, *ApJ*, **681**, 1183
 Kewley L. J., Maier C., Yabe K., Ohta K., Akiyama M., Dopita M. A., Yuan T., 2013, *ApJ*, **774**, L10
 Kewley L. J., Zahid H. J., Geller M. J., Dopita M. A., Hwang H. S., Fabricant D., 2015, *ApJ*, **812**, L20
 Kojima T., Ouchi M., Nakajima K., Shibuya T., Harikane Y., Ono Y., 2017, *PASJ*, **69**, 44
 Luridiana V., Morisset C., Shaw R. A., 2015, *A&A*, **573**, A42
 Ly C., Malkan M. A., Rigby J. R., Nagao T., 2016, *ApJ*, **828**, 67
 Maiolino R., et al., 2008, *A&A*, **488**, 463
 Neville M., Stensitzki T., Allen D. B., Ingargiola A., 2014, LMFIT: Non-Linear Least-Square Minimization and Curve-Fitting for Python, doi:10.5281/zenodo.11813, <https://doi.org/10.5281/zenodo.11813>
 Osterbrock D. E., 1989, *Astrophysics of gaseous nebulae and active galactic nuclei*
 Pagel B. E. J., Edmunds M. G., Blackwell D. E., Chun M. S., Smith G., 1979, *MNRAS*, **189**, 95
 Patrício V., et al., 2016, *MNRAS*, **456**, 4191
 Pérez-Montero E., 2014, *MNRAS*, **441**, 2663
 Pettini M., Pagel B. E. J., 2004, *MNRAS*, **348**, L59
 Pettini M., et al., 2010, *MNRAS*, **402**, 2335
 Pilyugin L. S., Vílchez J. M., Cedrés B., Thuan T. X., 2010, *MNRAS*, **403**, 896
 Rigby J. R., Wuyts E., Gladders M. D., Sharon K., Becker G. D., 2011, *ApJ*, **732**, 59
 Salpeter E. E., 1955, *ApJ*, **121**, 161
 Sanders R. L., et al., 2015, *ApJ*, **799**, 138
 Sanders R. L., et al., 2016, *ApJ*, **825**, L23
 Schlegel D. J., Finkbeiner D. P., Davis M., 1998, *ApJ*, **500**, 525
 Shaw R. A., Dufour R. J., 1995, *Publications of the Astronomical Society of the Pacific*, **107**, 896
 Stark D. P., et al., 2014, *MNRAS*, **445**, 3200
 Steidel C. C., et al., 2014, *ApJ*, **795**, 165
 Steidel C. C., Strom A. L., Pettini M., Rudie G. C., Reddy N. A., Trainor R. F., 2016, *ApJ*, **826**, 159
 Villar-Martín M., Cerviño M., González Delgado R. M., 2004, *MNRAS*, **355**, 1132
 Wisnioski E., et al., 2015, *ApJ*, **799**, 209
 Yuan T.-T., Kewley L. J., 2009, *ApJ*, **699**, L161

APPENDIX A: METALLICITY CALIBRATIONS

Here we list the metallicity calibrations used in this work. All calibrations from Maiolino et al. 2008, Jones et al. 2015 and Curti et al. 2017 are given as $\log_{10} R = \sum_n c_n x^n$, where R is the line ratio, c_n the calibration coefficients and x^n the metallicity in $12+\log(\text{O}/\text{H}) - 8.69$. For the Bian et al. 2018

calibrations, only $R23$, $O3$ and $Ne2O2$ are given in function of the metallicity, while $O32$, $N2$ and $O3N2$ are given in function of the line ratios (i.e. $12+\log(\text{O}/\text{H}) = p_0 + p_1 \log_{10} R$). In Table A1, A2 A3 and A4 we list all the coefficients for the different ratios used in this work.

APPENDIX B: LINE FLUXES

The line fluxes presented here are based in the values available in the literature (see Table 1). Using the literature fluxes, we have simultaneously derived extinction, electron temperature and density for each galaxy (see Table 2). We present the dust corrected fluxes in Table B1, which were used to calculate electron temperature and density and the corrected oxygen fluxes in Table 2. Table B2 shows the strong line ratios used to calculate metallicity using the strong line ratios method.

This paper has been typeset from a $\text{\TeX}/\text{\LaTeX}$ file prepared by the author.

Table A1. Maiolino et al. 2008 (M08) calibrations. The coefficients are listed in table 4 of that work and were derived with data ranging between 7 and 9.2 in $12+\log(\text{O}/\text{H})$.

R	c_0	c_1	c_2	c_3	c_4
<i>R23</i> $([\text{O II}] \lambda 3727,29 + [\text{O III}] \lambda 4959 + [\text{O III}] \lambda 5007) / \text{H}\beta$	0.7462	-0.7149	-0.9401	-0.6154	-0.2524
<i>O3</i> $[\text{O III}] \lambda 5007 / \text{H}\beta$	0.1549	-1.5031	-0.9790	-0.0297	-
<i>O2</i> $[\text{O II}] \lambda 3727,29 / \text{H}\beta$	0.5603	0.0450	-1.8017	-1.8434	-0.6549
<i>O32</i> $[\text{O II}] \lambda 3727,29 / [\text{O III}] \lambda 5007$	-0.2839	-1.3881	-0.3172	-	-
<i>O3N2</i> $[\text{O III}] \lambda 5007 / [\text{N II}] \lambda 6585$	0.4520	-2.6096	-0.7170	0.1347	-
<i>N2</i> $[\text{N II}] \lambda 6585 / \text{H}\alpha$	-0.7732	1.2357	-0.2811	-0.7201	-0.3330
<i>Ne2O2</i> $\text{Ne III} \lambda 3869 / [\text{O II}] \lambda 3727,29$	-1.2608	-1.0861	-0.1470	-	-

Table A2. Jones et al. 2015 (J15) calibrations, listed in table 1 of that work. The data used to derive this calibrations have metallicities from 7.6 to 9.0 in $12+\log(\text{O}/\text{H})$.

R	c_0	c_1	c_2
<i>R23</i> $([\text{O II}] \lambda 3727,29 + [\text{O III}] \lambda 4959 + [\text{O III}] \lambda 5007) / \text{H}\beta$	-54.1003	13.9083	-0.8782
<i>O3</i> $[\text{O III}] \lambda 5007 / \text{H}\beta$	-88.4378	22.7529	-1.4501
<i>O2</i> $[\text{O II}] \lambda 3727,29 / \text{H}\beta$	-154.9571	36.9128	-2.1921
<i>O32</i> $[\text{O II}] \lambda 3727,29 / [\text{O III}] \lambda 5007$	17.9828	-2.1552	-
<i>Ne2O2</i> $\text{Ne III} \lambda 3869 / [\text{O II}] \lambda 3727,29$	16.8974	-2.1588	-
<i>Ne2O3</i> $\text{Ne III} \lambda 3869 / [\text{O III}] \lambda 5007$	-1.0854	-0.0036	-

Table A3. Curti et al. 2017 (C17) calibrations. These coefficients are listed in table 2 of that work. The last column lists the range of applicability of each line ratio, as given by the authors.

R	c_0	c_1	c_2	c_3	c_4	Range
<i>R23</i> $([\text{O II}] \lambda 3727,29 + [\text{O III}] \lambda 4959 + [\text{O III}] \lambda 5007) / \text{H}\beta$	0.527	-1.569	-1.652	-0.421	-	$8.4 < 12+\log(\text{O}/\text{H}) < 8.85$
<i>O3</i> $[\text{O III}] \lambda 5007 / \text{H}\beta$	-0.277	-3.549	-3.593	-0.981	-	$8.3 < 12+\log(\text{O}/\text{H}) < 8.85$
<i>O2</i> $[\text{O II}] \lambda 3727,29 / \text{H}\beta$	0.418	-0.961	-3.505	-1.949	-	$7.6 < 12+\log(\text{O}/\text{H}) < 8.3$
<i>O32</i> $[\text{O II}] \lambda 3727,29 / [\text{O III}] \lambda 5007$	-0.691	-2.944	-1.308	-	-	$7.6 < 12+\log(\text{O}/\text{H}) < 8.85$
<i>O3N2</i> $([\text{O III}] \lambda 5007 / \text{H}\beta) / ([\text{N II}] \lambda 6585 / \text{H}\alpha)$	0.281	-4.765	-2.268	-	-	$7.6 < 12+\log(\text{O}/\text{H}) < 8.85$
<i>N2</i> $[\text{N II}] \lambda 6585 / \text{H}\alpha$	-0.489	1.513	-2.554	-5.293	-2.867	$7.6 < 12+\log(\text{O}/\text{H}) < 8.85$

Table A4. Bian et al. 2018 (BKD18) calibrations. The coefficients are listed in equations 11, 12 and 16 to 18 of that work. The first three calibrations are written in function of metallicity ($\log_{10} R = \sum_n c_n x^n$) and the last 3 in function of the line ratios ($12+\log(\text{O}/\text{H}) = p_0 + p_1 \log_{10} R$). The sample spans a metallicity range of $7.8 < 12+\log(\text{O}/\text{H}) < 8.4$.

R	c_0	c_1	c_2	c_3
<i>R23</i> $([\text{O II}] \lambda 3727,29 + [\text{O III}] \lambda 4959 + [\text{O III}] \lambda 5007) / \text{H}\beta$	138.0430	-54.8284	7.2954	-0.32293
<i>O3</i> $[\text{O III}] \lambda 5007 / \text{H}\beta$	43.9836	-21.6211	3.4277	-0.1747
<i>Ne2O2</i> $\text{Ne III} \lambda 3869 / [\text{O II}] \lambda 3727,29$	7.80	-0.63	-	-
R	p_0	p_1		
<i>N2</i> $[\text{N II}] \lambda 6585 / \text{H}\alpha$	8.82	0.49		
<i>O3N2</i> $([\text{O III}] \lambda 5007 / \text{H}\beta) / ([\text{N II}] \lambda 6585 / \text{H}\alpha)$	8.97	-0.39		
<i>O3</i> $[\text{O III}] \lambda 5007 / \text{H}\beta$	8.54	-0.59		

Table B1. Extinction corrected line fluxes, normalised to H β .

Obj	O III] λ 1661	O III] λ 1666	[C III] λ 1907	C III] λ 1909	Ne III] λ 3869	[O II] λ 3727,29	H δ
CSWA20	0.062 \pm 0.538	0.154 \pm 0.245	0.193 \pm 0.136	0.177 \pm 0.137	0.421 \pm 0.136	0.542 \pm 0.274	-
Abell_860_359	\leq 0.037	0.101 \pm 0.273	-	-	-	\leq 1.265	-
Abell_22.3	-	-	-	-	-	1.490 \pm 0.194	-
RCSGA	-	-	-	-	0.308 \pm 0.004	2.918 \pm 0.010	0.265 \pm 0.004
A1689_31.1	0.185 \pm 0.002	0.428 \pm 0.002	0.302 \pm 0.002	0.587 \pm 0.002	0.199 \pm 0.003	0.668 \pm 0.003	-
SMACS_0304	0.026 \pm 0.140	0.043 \pm 0.132	-	-	0.365 \pm 5.169	2.613 \pm 0.326	0.300 \pm 0.122
MACS_0451	0.243 \pm 0.099	0.364 \pm 0.102	-	-	-	\leq 0.645	-
COSMOS_12805	0.053 \pm 0.020	0.081 \pm 0.028	-	-	-	\leq 2.924	-
BX660	\leq 0.000	0.230 \pm 0.060	-	-	-	0.879 \pm 0.177	-
BX74	\leq 0.000	0.169 \pm 0.175	-	-	-	1.125 \pm 0.313	-
BX418	\leq 0.000	0.152 \pm 0.049	-	-	-	0.909 \pm 0.181	-
S16-stack	0.016 \pm 0.174	0.046 \pm 0.120	0.160 \pm 0.113	0.111 \pm 0.117	0.375 \pm 0.139	2.677 \pm 0.326	-
COSMOS-1908	-	-	-	-	0.426 \pm 0.040	0.509 \pm 0.045	0.338 \pm 0.047
Lynx arc	\leq 0.188	\leq 0.396	\leq 0.361	\leq 0.248	\leq 0.692	\leq 0.251	-
SMACS_2031	0.072 \pm 0.014	0.218 \pm 0.018	0.293 \pm 0.015	0.205 \pm 0.022	0.347 \pm 0.050	0.703 \pm 0.071	-
SGAS_1050	0.019 \pm 0.007	0.054 \pm 0.007	0.209 \pm 0.069	0.126 \pm 0.079	0.322 \pm 0.040	0.795 \pm 0.021	-

Table B1 – *continued*

Obj	H γ	[O III] λ 4364	H β	[O III] λ 4959	[O III] λ 5007	H α	[N II] λ 6585
CSWA20	0.611 \pm 0.150	0.053 \pm 0.356	1.000 \pm 0.174	1.651 \pm 0.237	4.886 \pm 0.614	2.869 \pm 0.371	0.052 \pm 0.217
Abell_860_359	-	-	1.000 \pm 0.096	2.022 \pm 0.152	6.083 \pm 0.420	2.821 \pm 0.201	-
Abell_22.3	-	0.310 \pm 0.149	1.000 \pm 0.142	1.933 \pm 0.222	6.225 \pm 0.634	3.703 \pm 0.386	\leq 0.037
RCSGA	0.474 \pm 0.004	\leq 0.052	1.000 \pm 0.005	1.489 \pm 0.006	4.753 \pm 0.016	2.720 \pm 0.010	0.173 \pm 0.004
A1689_31.1	0.463 \pm 0.003	0.168 \pm 0.003	1.000 \pm 0.003	1.438 \pm 0.004	4.771 \pm 0.011	-	-
SMACS_0304	0.458 \pm 0.129	-	1.000 \pm 0.165	1.315 \pm 0.192	4.591 \pm 0.547	2.868 \pm 0.352	0.092 \pm 0.114
MACS_0451	-	-	1.000 \pm 0.136	1.368 \pm 0.140	3.943 \pm 0.381	2.541 \pm 0.288	\leq 0.064
COSMOS_12805	-	-	1.000 \pm 0.418	1.889 \pm 0.694	6.456 \pm 1.928	2.824 \pm 0.836	\leq 0.099
BX660	-	-	1.000 \pm 0.277	3.198 \pm 1.005	6.395 \pm 1.289	2.751 \pm 0.574	\leq 0.070
BX74	-	-	1.000 \pm 0.341	2.449 \pm 0.726	7.799 \pm 1.889	3.097 \pm 0.760	0.107 \pm 0.210
BX418	-	-	1.000 \pm 0.278	2.299 \pm 0.822	6.395 \pm 1.290	2.792 \pm 0.582	0.149 \pm 0.042
S16-stack	-	\leq 0.066	1.000 \pm 0.162	1.434 \pm 0.200	4.255 \pm 0.499	2.866 \pm 0.346	0.277 \pm 0.117
COSMOS-1908	0.491 \pm 0.043	0.124 \pm 0.049	1.000 \pm 0.047	2.270 \pm 0.081	6.973 \pm 0.232	-	-
Lynx arc	-	-	\leq 1.000	\leq 2.579	\leq 7.497	-	-
SMACS_2031	-	-	1.000 \pm 0.049	1.446 \pm 0.054	4.792 \pm 0.166	-	-
SGAS_1050	0.521 \pm 0.020	\leq 0.014	1.000 \pm 0.014	2.349 \pm 0.030	8.076 \pm 0.082	-	-

Table B2. Strong line ratios used to calculate the metallicities in Section 5 and 6 (in \log_{10} scale). † Both $H\beta$ and $[O\ II] \lambda 3727, 29$ are upper limits, so it is not possible to reliably calculate uncertainties.

Obj	$R23$	$N2$	$O3$	$O32$	$O2$	$O3N2$	$Ne3O3$	$Ne3O2$
CSWA20	$0.848^{+0.063}_{-0.053}$	$-1.277^{+0.313}_{-0.517}$	$0.686^{+0.064}_{-0.055}$	$0.926^{+0.232}_{-0.151}$	$-0.233^{+0.161}_{-0.259}$	$1.526^{+0.524}_{-0.317}$	$-0.121^{+0.257}_{-0.133}$	$-1.055^{+0.122}_{-0.219}$
Abell_860_359	$0.971^{+0.039}_{-0.033}$	-	$0.782^{+0.039}_{-0.032}$	$0.683^{+0.005}_{-0.006}$	≤ 0.098	-	-	-
Abell_22.3	$0.975^{+0.053}_{-0.044}$	≥ -2.003	$0.808^{+0.049}_{-0.047}$	$0.776^{+0.135}_{-0.107}$	$0.026^{+0.121}_{-0.129}$	$2.111^{+0.020}_{-0.023}$	-	-
RCSGA	$0.963^{+0.001}_{-0.001}$	$-1.196^{+0.008}_{-0.009}$	$0.676^{+0.001}_{-0.001}$	$0.204^{+0.001}_{-0.001}$	$0.471^{+0.001}_{-0.001}$	$1.450^{+0.008}_{-0.008}$	$-0.977^{+0.004}_{-0.004}$	$-1.181^{+0.005}_{-0.004}$
A1689_31.1	$0.837^{+0.001}_{-0.001}$	-	$0.680^{+0.001}_{-0.001}$	$0.871^{+0.002}_{-0.002}$	$-0.190^{+0.002}_{-0.002}$	-	$-0.526^{+0.009}_{-0.007}$	$-1.397^{+0.009}_{-0.007}$
SMACS_0304	$0.934^{+0.049}_{-0.054}$	$-1.382^{+0.263}_{-0.411}$	$0.666^{+0.044}_{-0.056}$	$0.242^{+0.024}_{-0.023}$	$0.420^{+0.051}_{-0.056}$	$1.590^{+0.416}_{-0.271}$	$0.137^{+0.314}_{-0.505}$	$-0.089^{+0.295}_{-0.502}$
MACS_0451	$0.774^{+0.042}_{-0.042}$	≥ -1.599	$0.596^{+0.042}_{-0.042}$	$0.797^{+0.006}_{-0.005}$	≥ -0.201	$1.783^{+0.006}_{-0.005}$	-	-
COSMOS_12805	$1.053^{+0.174}_{-0.116}$	≥ -1.453	$0.809^{+0.171}_{-0.109}$	$0.347^{+0.020}_{-0.020}$	≤ 0.462	$1.809^{+0.020}_{-0.020}$	-	-
BX660	$1.028^{+0.100}_{-0.095}$	≥ -1.598	$0.811^{+0.099}_{-0.079}$	$0.866^{+0.030}_{-0.028}$	$-0.059^{+0.101}_{-0.079}$	$1.960^{+0.021}_{-0.021}$	-	-
BX74	$1.048^{+0.100}_{-0.065}$	$-1.211^{+0.261}_{-0.572}$	$0.880^{+0.093}_{-0.065}$	$0.801^{+0.057}_{-0.051}$	$0.083^{+0.102}_{-0.091}$	$1.636^{+0.585}_{-0.244}$	-	-
BX418	$0.972^{+0.099}_{-0.087}$	$-1.085^{+0.240}_{-0.511}$	$0.790^{+0.108}_{-0.081}$	$0.846^{+0.044}_{-0.045}$	$-0.050^{+0.097}_{-0.097}$	$1.452^{+0.494}_{-0.253}$	-	-
S16-stack	$0.920^{+0.053}_{-0.043}$	$-1.045^{+0.170}_{-0.223}$	$0.620^{+0.055}_{-0.043}$	$0.183^{+0.021}_{-0.021}$	$0.438^{+0.054}_{-0.044}$	$1.230^{+0.223}_{-0.164}$	$-0.863^{+0.137}_{-0.161}$	$-1.048^{+0.136}_{-0.159}$
COSMOS-1908	$0.989^{+0.016}_{-0.015}$	-	$0.844^{+0.016}_{-0.015}$	$1.134^{+0.036}_{-0.032}$	$-0.291^{+0.037}_{-0.039}$	-	$-0.086^{+0.057}_{-0.041}$	$-1.218^{+0.038}_{-0.047}$
Lynx arc	≤ 1.014	-	≤ 0.875	$1.477^{+0.017}_{-0.015}$	-0.602^\dagger	-	$0.461^{+0.134}_{-0.241}$	$-1.020^{+0.141}_{-0.244}$
SMACS_2031	$0.840^{+0.018}_{-0.016}$	-	$0.680^{+0.016}_{-0.015}$	$0.837^{+0.042}_{-0.038}$	$-0.156^{+0.043}_{-0.048}$	-	$-0.302^{+0.073}_{-0.067}$	$-1.137^{+0.052}_{-0.075}$
SGAS_1050	$1.050^{+0.005}_{-0.004}$	-	$0.907^{+0.005}_{-0.004}$	$1.009^{+0.012}_{-0.010}$	$-0.102^{+0.012}_{-0.013}$	-	$-0.388^{+0.048}_{-0.059}$	$-1.398^{+0.046}_{-0.062}$

Table B3. Accuracy of the calibrations measured by the mean (\bar{x}) and standard deviation ($\sigma_{z \sim 2}$) of the residuals $12+\log(O/H)_{calib} - 12+\log(O/H)_{Te}$, where the first is the metallicity obtained with that particular calibration and diagnostic and the second from the T_e method. The number of objects used to test each calibration are listed in the "#" columns. The intrinsic dispersion ($\sigma_{int.}$) from Jones et al. 2015 and Curti et al. 2017 obtained at $z \sim 0$ and up to $z \sim 0.8$ respectively, is also listed for comparison. The last row lists the absolute mean of both \bar{x} and $\sigma_{z \sim 2}$ for each calibration.

	Maiolino et al. 2008			Jones et al. 2015				Curti et al. 2017			Bian et al. 2018			
	#	\bar{x}	$\sigma_{z \sim 2}$	#	\bar{x}	$\sigma_{z \sim 2}$	$\sigma_{int.}$	#	\bar{x}	$\sigma_{z \sim 2}$	$\sigma_{int.}$	#	\bar{x}	$\sigma_{z \sim 2}$
$R23$	12	-0.04 ± 0.06	0.21 ± 0.03	15	0.15 ± 0.07	0.30 ± 0.07	0.06	15	0.03 ± 0.06	0.22 ± 0.05	0.12	15	0.29 ± 0.10	0.36 ± 0.07
$N2$	10	0.13 ± 0.07	0.23 ± 0.04	-	-	-	-	10	0.15 ± 0.07	0.21 ± 0.05	0.10	10	0.16 ± 0.06	0.19 ± 0.05
$O3$	13	-0.08 ± 0.06	0.19 ± 0.03	14	0.16 ± 0.08	0.30 ± 0.05	0.10	13	0.04 ± 0.05	0.20 ± 0.05	0.07	16	0.31 ± 0.09	0.39 ± 0.07
$O32$	16	-0.24 ± 0.11	0.41 ± 0.06	16	0.05 ± 0.07	0.27 ± 0.05	0.23	16	-0.01 ± 0.08	0.33 ± 0.06	0.14	16	0.15 ± 0.07	0.28 ± 0.05
$O2$	16	0.23 ± 0.06	0.24 ± 0.04	15	0.06 ± 0.06	0.25 ± 0.04	0.15	16	-0.01 ± 0.06	0.25 ± 0.05	0.26	-	-	-
$O3N2$	10	0.15 ± 0.07	0.21 ± 0.05	-	-	-	-	10	0.19 ± 0.06	0.21 ± 0.06	0.09	10	0.16 ± 0.06	0.21 ± 0.06
$Ne3O2$	9	-0.15 ± 0.17	0.48 ± 0.06	9	0.02 ± 0.09	0.27 ± 0.06	0.22	-	-	-	-	9	-0.01 ± 0.11	0.36 ± 0.07
mean		0.15	0.28		0.09	0.28			0.07	0.24			0.18	0.30